# Modeling cratered surfaces with real and synthetic terrain for testing planetary landers

Martin, Iain; Parkes, Stephen (Steve); Dunstan, Martin

*Published in:*
IEEE Transactions on Aerospace and Electronic Systems

*DOI:*
10.1109/TAES.2014.120282

*Publication date:*
2014

*Document Version*
Peer reviewed version

# Modeling Cratered Surfaces with Real and Synthetic Terrain for Testing Planetary Landers

Iain Martin, Steve. Parkes, *Member, IEEE*, and Martin Dunstan

***Abstract*— The autonomous guidance of a spacecraft lander requires extensive testing to develop and prove the technology. Methods such as machine vision for navigation and both vision and LIDAR for hazard avoidance are being studied and developed to provide precise, robust lander guidance systems. A virtual test environment which can simulate these instruments is a vital tool to aid this work. When available, terrain elevation models can provide a base for simulation but they frequently contain artifacts, gaps or may not have the required resolution. We propose novel techniques to model heavily cratered surfaces for testing planetary landers by combining crater models and fractal terrain to create a multi-resolution mesh for simulating a spacecraft descent and landing. The synthetically enhanced models are evaluated by comparing enhanced terrain based on Clementine/RADAR data with higher resolution terrain models from Selene and Lunar Reconnaissance Orbiter to show that the artificial models are suitable for testing planetary lander systems.**

***Index Terms*—Crater Modeling, Fractal Terrain Generation, Lunar Landing**

## I. Introduction

### A. *Autonomous planetary landers*

The autonomous guidance of a spacecraft down to a pre-designated target landing spot avoiding small craters or other obstacles in the vicinity of the landing site is a difficult task. Vision-based navigation techniques and vision and LIDAR-based obstacle avoidance techniques are being studied and developed to provide precise, robust lander guidance, so require extensive testing. Ideally a test environment covering the full descent sequence is required, with characteristics that are close to the planet to be landed on, which can be modified quickly to support repeated tests on similar but different terrain and which has lighting and atmospheric conditions like the target planet. Such a test system is not practical unless virtual reality techniques are adopted and virtual planets and spacecraft are developed [1]. Other possible test environments include helicopter flight-testing on Earth and physical mock up terrain imaged using a camera mounted on a robotic arm. However, these systems are high cost and suffer from problems such as calibration and recreating the lighting and atmospheric effects that the space craft lander would encounter [2]. A major challenge in simulating a lander descent is the model resolution range required from kilometers at the start of the descent to centimeters at the landing site. This paper describes a novel crater model to simulate crater saturated terrain and presents a framework to show how this crater model can be used with other terrain modeling techniques to generate multi-resolution models to simulate spacecraft descent and landing to test navigation and guidance systems.

Manuscript received MON-DD-YYYY; revised MON-DD-YYYY. This work was supported in part by the European Space Agency Contracts; PANGU (ESA Contract No. 11747/95/NL/JG) and PANGU Extension (ESA Contract No. 20858/07/NL/EK).

I. Martin, S. Parkes and M. Dunstan are at the Space Technology Centre, University of Dundee, UK e-mail: imartin@computing.dundee.ac.uk.

### B. *Lunar South Pole Lander*

The lunar South Pole is selected as an example region to demonstrate the surface modeling techniques presented in this paper although the results can be extrapolated to simulate any rocky, cratered surface. It is an area of high interest for lunar scientists and mission planners because of the potential for water ice in shadowed craters and well illuminated areas for target landing sites [3]. The European Space Agency (ESA) has instigated a study program to demonstrate key technologies for a robotic lunar South Pole lander scheduled to launch in 2018 [4]. A stated goal is a precise, automated lander to land within 200 m of a target on one of the near constantly illuminated regions near the South Pole [5] where analysis of topographic data estimate the size of the well illuminated landing sites to be in the order of 100's of meters [6]. To prove the technology for such a precise autonomous lander, it is therefore important to exhaustively test the navigation, guidance and hazard avoidance systems.

### C. *The Lunar Surface*

The Moon has been studied extensively from Earth-based telescopes and radar, manned and unmanned landers (the Luna, Ranger and Surveyor and Apollo missions in the 1960's) and by remote sensing from orbiting spacecraft, such as Clementine in 1994, Lunar Prospector in 1998, Selene in 2007 and the current Lunar Reconnaissance Orbiter (LRO). On rocky, solid planetary bodies with no atmosphere, impact cratering is generally the dominant geological process with the Moon, Mercury and most asteroids having heavily cratered surfaces. Impact craters have a similar form on all rocky planetary bodies with some variance due to surface density and gravitational strength [7]. Craters are classified as simple or complex with simple craters having bowl shaped interiors with intact rims. Craters larger than the simple/complex transition diameter have flatter bottoms, collapsed rims and may have central uplift. Lunar simple craters have diameters ranging from micrometers to ~10-15 km. Fresh simple craters

have a nearly parabolic interior, a sharp raised rim and an ejecta blanket, which slopes down, radially out from the rim [8]. Larger craters have more complex forms and may contain features such as, a flat bottom, rim terraces, central peaks and interior rings [7]. The smoother Mare regions are estimated to be saturated with impact craters below 200 m in diameter [9] and the rougher highland regions saturated below 1.2 km [10].

There is little modern published material on crater degradation but Ross [11] and Soderblom [12] created separate models of lunar crater degradation based on topographic displacement caused by small meteorite impacts. They showed that as craters degrade the crater rim height and depth reduce due to surface creep and infill from small settling particles leading to shallower craters with rounded rims. A severely eroded crater will appear as a depression with no rim.

## II. Related Work

### A. *Synthetic Terrain Modeling*

There are a variety of standard techniques that can be used to generate synthetic terrain, mostly based on fractals, simulating fractional Brownian motion (fBm) in two dimensions to generate elevation models of rocky terrain [13]. Terrain roughness can be controlled by setting the fractal dimension and constraints can be set by specifying initial height values but this often leads to spike artifacts. Millar [14] describes Random Mid-point Displacement algorithms (RMD) and explains their limitations when constraints are imposed. A widely used RMD algorithm is the 'diamond-square' algorithm which calculates new (child) elevation values by interpolating known (parent) values in diamond and square phases [14]. New height values are calculated in a fixed pattern which limits which Digital Elevation Model (DEM) height values can be constrained and artifacts can form when initial values are defined from known height values. Belhadj proposes the Morphologically Constrained Midpoint Displacement (MCMD) algorithm [15] which can fill DEM gaps where the order and position of constrained values are not restricted to a set pattern of initial parents as would be required with standard RMD. MCMD may be the preferred algorithm for modeling surfaces with mountains and ridges, or from sparse DEMs with irregularly spaced known height values but was less suitable for lunar DEM interpolation because many of the gaps were crater interiors which would not be modeled realistically with this technique.

Perlin noise [16] can be used to generate fractal terrain by summing different octaves of noise functions and can be evaluated at any position without reference to neighboring points which allows increasing level of detail to be calculated with higher frequency noise octaves. This approach would be advantageous if a purely synthetic model was required but is less suitable for combining with real terrain because it is difficult to blend the noise functions with existing known height values without altering the known heights.

Vasudevan describes Gaussian process modeling of terrain [17] to model unknown sections of terrain which could be applied to fill gaps in elevation models or interpolate to increase resolution and Zhou describes a technique to add new terrain from defined patches, focusing on ridges and valleys but like many terrain generation techniques they are not directly applicable for simulating or expanding lunar terrain because they don't simulate crater saturated terrain [18] with craters included at all resolutions.

### B. *Cratered surface modeling*

Previous research in lunar surface modeling has added impact craters to terrain to simulate crater saturated surfaces. Hartmann [10] adds large numbers of fresh bowl shaped craters to flat terrain in phases with smoothing between each phase to track the evolution of surface morphology as new craters are formed. The generated surfaces have comparable slope distributions to lunar terrain but are not realistic due to excessively sharp edged craters, unrealistic crater overlaps and blurred terrain caused by the smoothing filter. Shankar [19] created synthetic lunar terrain by separating the low and high frequency terrain, scooping out crater shaped regions from the low frequency terrain then adding back the high frequency which achieves a realistic texture but the overlapping craters are unrealistic and crater degradation was not considered. Qinghua [20] presents a Genetic Algorithm approach to generating terrain with similar spatial and slope characteristics to lunar terrain but the surfaces generated are not visually similar to real terrain. A more realistic lunar terrain model was created by Huang [21] who added crater models to a fractal terrain created by the square-square RMD algorithm which generated a realistic base terrain but the crater model did not include crater degradation. The common approach in the related work is to simulate the crater saturated lunar surface by adding craters to fractal surfaces with realistic diameter distributions. This approach could be significantly improved with a more realistic crater model that could be blended into existing terrain and be combined with real elevation data where available.

## III. Crater Modeling

Craters are formed by high energy impacts which obliterate the crater bowl region and throw out an ejecta blanket of material radially outwards from the crater. A novel crater model based on the form of simple craters was developed to simulate individual impacts and crater saturated terrain. It combines idealized mathematical crater profiles with fractal techniques to produce a realistic form. The advances over previous crater models are to include crater degradation and to smoothly integrate craters into the surrounding terrain so that overlapping craters and crater saturated terrain can be simulated.

### A. *Radial profile*

A crater radial profile was developed from four connected polynomials representing height at a normalized radial distance from the crater center. Polynomials were used because fresh crater bowl and rim equations are defined as polynomials in the literature [7] and the degraded rim shown from Ross's model [11] can also be reasonably approximated

by constrained polynomials. The obliteration region is modeled by defining a plane (see Figure 1) to represent the average slope of the crater bowl impact region. Terrain heights in the crater bowl are calculated as the sum of the bowl height and the plane while in the ejecta they are defined as the sum of the underlying terrain, the ejecta model and a corrective function to match the ejecta to the rim and the surrounding terrain at the edge of the ejecta as shown in Figure 2.

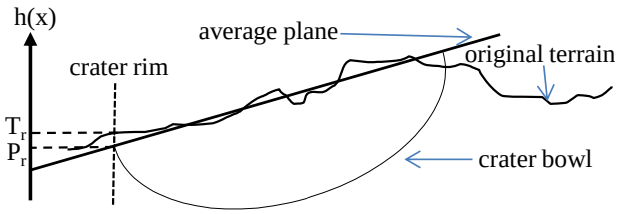


Figure 1: Definition of a plane to represent the obliterated crater interior

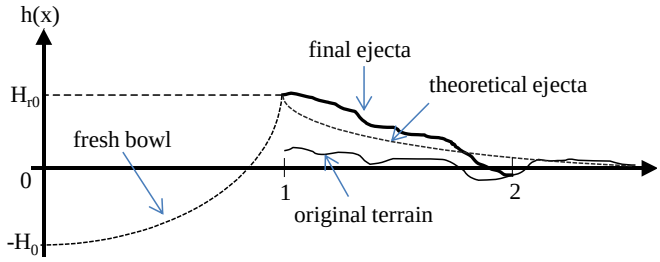


Figure 2: Crater model profile showing the blending of the idealized ejecta with the surrounding terrain

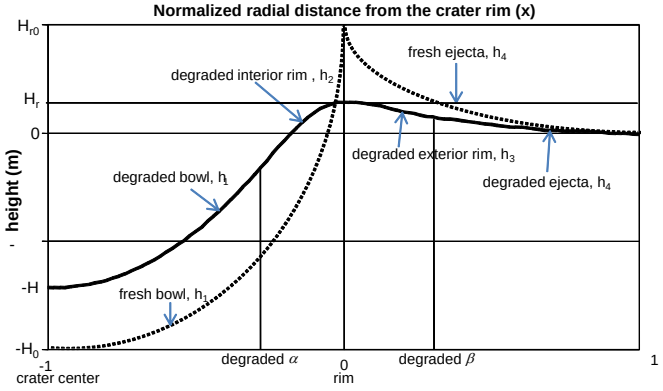


Figure 3: Fresh and degraded crater profiles

The crater bowl, $h_1$, is defined as a quadratic to model the interior bowl shape as specified by Melosh and the ejecta, $h_4$, by the profile given by McGetchin [22]. The two additional polynomials, $h_2$, $h_3$, are defined to smoothly connect the interior to the rim to simulate the degradation of the crater with a rounded rim to model the form of degraded craters defined by Ross [25]. The radial distance α is defined as the point where the crater bowl joins the interior rim, and β defines where the ejecta joins the exterior rim. The polynomials are constrained by defining the height at the crater center to be the crater depth, at the rim to be the crater rim height, the edge of the ejecta to be zero, the interior crater rim to match the exterior crater rim at the rim center with a gradient of zero and at points α and β, the values, first and second derivatives of the connecting polynomials to match. The polynomial coefficients are determined by solving for these constraints.

The four polynomials are given below and use the following definitions. $H_0$ and $H_{r0}$ (see Figure 3) define the fresh crater depth and rim height in relation to diameter, *D*. Melosh [7] defines $H_0$ and $H_{r0}$ for fresh lunar craters as

**(1)** $H_0 = 0.196D^{1.01}$, and

**(2)** $H_{r0} = 0.036D^{1.01}$.

$H$ and $H_r$ define the depth and rim height of the eroded crater and are calculated by multiplying $H_0$ and $H_{r0}$ by a normalized erosional factor representing crater degradation. $T_r$ is the height of the terrain at the crater rim along the current radius and $P_r$ represents the height of the plane at the crater rim (see Figure 1). When $H_0 = H$ and $H_{r0} = H_r$, the crater is fresh and α and β are both at the rim. The greater the difference between the original crater depth and rim heights to actual crater depth and rim heights, the more eroded the crater is, α tends towards the crater center and β tends outwards which matches Ross's model of crater erosion [11]. To simplify solving for the coefficients, we define *x* as the normalized radial distance where *r* is the radial distance from the center of the crater.

**(3)** $x = \frac{2r}{D} - 1,\ -1 \le x \le 1.$

Equation (4) defines the parabolic crater bowl quadratic between the crater center and α.

**(4)** $h_1(x) = (H_{r0} - H_r + H)x^2 + 2(H_{r0} - H_r + H)x + H_{r0},\ -1 \le x \le \alpha$

Equation (5) represents the interior rim quadratic between α and the crater rim.

**(5)** $h_2(x) = \frac{(H_{r0} - H_r + H)(\alpha + 1)}{\alpha}x^2 + H_r + T_r - P_r,\ \alpha \le x \le 0$

Equation (6) defines the joining point between the crater bowl and the interior rim equations.

**(6)** $\alpha = \frac{H_r + T_r - P_r - H_{r0}}{H_{r0} - H_r + H}$

Equation (7) specifies the exterior rim cubic defined between the crater rim and β.

**(7)** $h_3(x) = \left(-\frac{2(H_{r0} - H_r + H)}{3\beta^2}\right)x^3 + \left((H_{r0} - H_r + H) + \frac{2(H_{r0} - H_r + H)}{\beta}\right)x^2 + H_r + T_r - P_r, 0 \le x \le \beta$

Equation (8) defines the joining point between the exterior rim and the ejecta equations.

**(8)** $\beta = \frac{3(H_r + T_r - P_r - H_{r0})}{2(H_{r0} - H_r + H)}$

Equation (9) defines the idealized ejecta blanket between β and the ejecta edge as specific by McGetchin [22] plus a corrective function ($F_c$) to seamlessly join the ejecta blanket to both the exterior rim of the crater and the surrounding surface

with $E_{min}$ representing the height of the ejecta at $x=D/2$.

**(9)** $h_4 = 0.14\left(\frac{D}{2}\right)^{0.74}(x+1)^{-3} + F_c,\ \beta \le x \le 1,$

**(10)** $F_c = (E_{\min} + T_r - P_r)x + 2(P_r - T_r) - E_{\min}$

Figure 3 shows the radial profiles of a fresh and a partially degraded crater, plotting height against radial distance from the center. The fresh crater profile is shown as a dashed plot and has a sharp rim with α and β are 0 so the interior bowl meets the ejecta at the rim. The degraded profile shows α moving inwards and β outwards giving a rounded rim.

To add realistic roughness to the crater a fractal surface is superimposed onto the new crater with fractal dimension defined as a function of radius from the crater center, creating radial fractal regions which specify the roughness and vertical height range of the fractal overlay. This controls the roughness of the floor of the crater, the wall of the crater and the ejecta blanket which appears rough near the rim of the crater. The ejecta region is generated as rough terrain but the amplitude is decreased linearly to zero from the rim to the end of the ejecta blanket to blend in with the surrounding terrain.

Most simple craters on the Moon are not perfectly circular. Uneven slopes, varying surface materials and surface strength can cause differing crater rim slumping resulting in irregular crater rims so the model was extended to incorporate a varying radius. A one-dimensional fractal array is created with matching start and end values to create a varying radius, filtered and scaled to a fraction of crater diameter.

### B. *Crater Degradation Based on Erosion*

If the erosional characteristics of a crater of a specific diameter are known then the relationship in Equation (11), given by both Ross [11] and Soderblum [12], can be used to extrapolate the crater degradation process to craters of all diameters to determine the crater depth and rim height reduction from a given age. If the age of a crater of an arbitrary diameter, $D_x$, is specified as $T_x$, then the time taken for the baseline crater with diameter $D_b$ to reach the same erosional state is $T_b$. The surface densities of the baseline and arbitrary craters are specified by $\sigma_b$ and $\sigma_x$. Unless there is a known difference in planetary surface materials between the baseline crater and other craters then it is reasonable to define the relative surface density as 1.0. Soderblom estimates that $P$ lies between 1.0 and 1.2 [12].

**(11)** $T_b = T_x\left(\frac{\sigma_b}{\sigma_x}\right)\left(\frac{D_b}{D_x}\right)^P$

The normalized crater depth and height values are calculated from baseline crater depth and rim height degradation profiles which define normalized crater depth and rim height with respect to $T_b$. A baseline erosion profile was not available from the literature so instead the outline figures from Ross's model [11] were used. The normalized crater depth and rim height values are applied as an erosion factor against $H_0$ and $H_{r0}$ for each crater.

### C. *Creating Cratered Surfaces*

Crater saturated surfaces can be generated by applying large numbers of craters in realistic diameter and age distributions, positioned randomly on the base surface. Lunar crater cumulative diameter-frequency distributions are available in the literature in the form $N_{cum}=cD^k$ where $N_{cum}(D)$ is the number of craters per unit area greater than a given diameter. The power $k$ is approximately −1.8 for lunar mare regions and -2.0 for a dimensionless surface with the crater population appearing similar at all resolutions. The number of craters per unit area within a specific diameter range can be calculated as:

**(12)** $N_{cum}(D_{min}, D_{max}) = N_{cum}(D_{min}) - N_{cum}(D_{max}).$

The constant c can be calculated when the range of crater diameters is defined and the cumulative frequency values for the range of crater diameters is known [7].

Craters should be added in age order to simulate the impact history of the surface. Age distributions are not available from the literature so a simple linear age distribution was used but this could be updated should the data become available. Figure 4 shows a rendered image from a purely synthetic model where the crater model has been added to a fractal surface with a lunar mare crater diameter distribution. This shows craters with different erosional states, regular and irregular rims and overlapping craters. The fractal surface and the fractal crater overlays were created using RMD with a fractal dimension of 2.2.

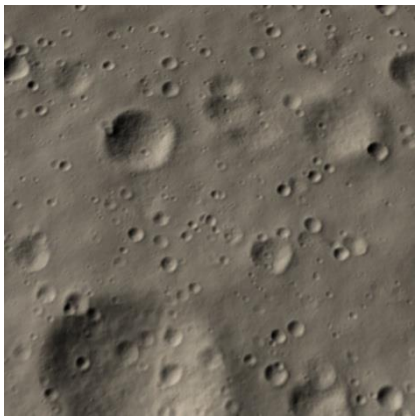

Figure 4: Synthetic lunar terrain

## IV. COMBINING REAL AND SYNTHETIC TERRAIN

The crater model defined in the previous section allows us to generate crater saturated surfaces that could be useful for testing spacecraft landers. However, for many missions, it is likely that real terrain data will be available so it may be advantageous to use this where possible but add synthetic terrain where there are gaps in the available elevation models or where higher resolution is required.

### A. *Fractal expansion of DEMs*

To provide a model to simulate a lander descent, a wide scale range may be required, with resolution varying from greater than a kilometer to less than a meter, covering an area of several hundred square kilometers around the target landing site [2]. This would be difficult to model in a single resolution because of the excessive amount of computer memory

required. To enable this range of resolution, a multi-resolution polygon mesh model can be created from a nested hierarchy of DEM layers with increasing resolution, tailored to the specifics of the lander scenario to be modeled. RMD type algorithms were chosen to create synthetic terrain to fill DEM gaps and to increase resolution because new terrain can be generated from existing height values without altering the originals. To model the landing site region with terrain representative of the planet's surface, realistic crater models are also required to add realistic high resolution features when expanding low resolution DEMs. We acknowledge that other terrain generation techniques may be equally appropriate for this stage if they could be combined with a crater model to create synthetic craters at higher resolutions. a

The RMD diamond-square algorithm generates square DEMs with pixel width sizes, *W*, where,

**(13)** $W = 2^{M+1}, \mathrm{M} \in \{1,2,3, \dots\}.$

To double the resolution of a region inside a DEM, a new DEM is created twice the pixel size of the region to expand, *2W*, with alternate pixels populated with values from the existing DEM. The gaps are filled by interpolating surrounding pixels in a square and diamond phase as shown in Figure 5.

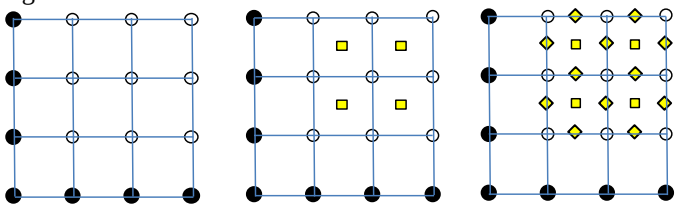

Figure 5: DEM fractal expansion

The filled circles denote pixels in the low resolution DEM only. The unfilled circles are in both DEMs and are copied directly. The square pixels are interpolated from the four surrounding known values in the square phase of RMD. The diamond pixels are interpolated from the two nearest circles and the two nearest squares in the diamond phase except for the border pixels which use the nearest pixels in the low resolution DEM to calculate a weighted average instead of the missing square.

The interpolated values are displaced by a random Gaussian scaled to approximate fBm as defined by Peitgen [23]. The scale is reduced after each square and diamond iteration to smoothly decrease the scale of the added random displacement variable between iterations. If *F* represents the Fractal Dimension which controls the surface roughness of the new terrain, then the scale factor, $S_f$, is calculated as

**(14)** $S_f = \frac{1}{2^{((3-F)/2)}}$

The initial scale factor, *S*, is given in Equation (4) where *H* is the height range scaling factor (in relation to the DEM size) and $D_r$ is the DEM horizontal resolution.

**(15)** $S = S_f . H . D_r . W . \sqrt{1 - 2^{(2(3-F)-2)}}$

The scale of the random additions of the new height points in the expanded DEM, $S_e$, can be calculated from the number of random mid-point displacement iterations required to reach the point before interpolating the new higher resolution values and an estimation of the fractal dimension of the base DEM, i.e. this calculates the scale of the random displacement at the final square and diamond iterations if the DEM was created entirely by RMD.

**(16)** $S_e = S . S_f{}^{(2M+1)}$

The DEM expansion process can be performed repeatedly to create regions of significantly higher resolution, creating an array of fractally expanded DEMs. This technique can be combined with the crater model by generating a list of crater definitions for the entire area and sorting it into separate lists for each DEM layer where craters are included in the highest resolution DEM layer that can include the complete crater and craters smaller than the DEM pixel resolution are rejected. Craters are added to each DEM layer before the expansion of the next highest resolution layer.

### B. *Filling gaps with fractal terrain*

Raw DEMs obtained from RADAR, laser altimeters or stereo matching often contain noise and gaps where data is unavailable. Replacing unknown height values with interpolation of surrounding known values creates unrealistically smooth terrain and sometimes obvious artifacts. Filling these gaps with realistic terrain or feature models could produce DEMs more representative of the actual planetary surface than filling gaps by simple interpolation.

A general DEM filling algorithm was created to fill gaps with fractal terrain. The DEM is scanned and all unknown pixels are added to a list. The number of known neighbors for each unknown pixel is calculated and used to order the list. Pixels with the most number of known neighbors are filled first and removed from the list. The number of known neighbors is recalculated for all unknown pixels and the list re-sorted accordingly. This process is repeated until all the unknown pixels are filled. This fills gaps from the outside inwards.

An individual hole pixel is filled by defining the new value as a weighted average of the nearest neighboring pixels in all eight directions plus a random unit Gaussian scaled by the roughness parameter and the DEM horizontal resolution. The weighting is the inverse of the pixel distance to the known value pixel.

### C. *Filling partial crater gaps*

Some gaps in lunar DEMs are the interior of craters that were obscured from the sensor by the surrounding raised crater rim so a technique was developed to replace unknown values which could be manually identified as the interior of a crater. The position and diameter of craters that obviously include gaps are manually defined and then a copy is made of the DEM. Two lists of unknown pixels are created, one containing all the unknown pixels inside craters rims and another containing all the unknown pixels. The unknown pixels in crater regions are filled with fractal terrain and the craters are added resulting in a DEM copy with all crater gaps filled with craters that do not smoothly match the surrounding terrain. The list of all unknown pixels inside crater regions is then sorted in order of number of known immediate neighbors.

The list is traversed and for each point, the height value in the DEM copy is copied to the original DEM, warped to ensure it blends in with the surrounding terrain. The warp method creates a weighted average of the nearest known points in the original DEM in all directions with the weighting being the inverse of the distance to the known point from the current point being filled. Unknown pixels in the original DEM are set to corresponding pixels in the DEM copy plus the warp value which blends the filled crater region smoothly into the surrounding terrain. An example of crater gap filling is shown in Figure 7.

### D. *Crater replacement*

The crater hole filling technique can be extended to replace craters which appear blurred from repeated fractal expansion in a multi-resolution model with synthetic versions that are resolution scalable so can appear sharp and realistic in high resolution regions of the model. All pixels in the crater bowl region are set to be unknown and then filled with fractal terrain. The crater is added to the highest resolution layer that can include the whole crater and the terrain points are propagated up to lower resolution DEMs so that the layers match exactly. Figure 6 shows an example from the South Pole model (described in the next section) where a replaced crater shows the sharp rim features which were lost with the excessive fractal expansion.

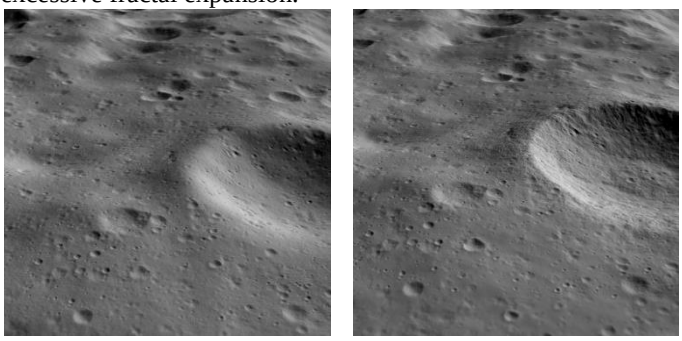

Figure 6: Rendered image of Shackleton crater from an fractally expanded model and with Shackleton replaced by a synthetic version in the same model.

## V. Results and Evaluation

The novel crater model and DEM enhancement techniques were evaluated by comparing two synthetically enhanced models to unenhanced models from Selene and LRO data to show that the techniques presented create realistic terrain. The aim is not to produce a terrain model identical to the terrain (which is unknown) but to produce plausible, high-resolution terrain where that data is not available or the DEM resolution is too low. The rendered images need to be realistic enough to be to be treated similarly by navigation and hazard detection image processing algorithms to simulate descent sequences for testing, developing and training autonomous planetary lander navigation and hazard avoidance systems. Slope distributions of the synthetically enhanced model were compared with lunar slope distributions from Apollo data, from unenhanced DEMs and at different resolutions in the enhanced model to evaluate slope consistency in the multi-resolution model. Finally, a typical navigation image processing algorithm is applied to real and synthetic models to evaluate the results.

### A. *Lunar Data Sets*

Three different lunar South Pole region data sets were used;

1. Clementine [24] / Earth based Radar fused model [25],
2. Kaguya (Selene) laser altimeter [6], and
3. LRO: Lunar Orbiter Laser Altimeter (LOLA) [26].

The Clementine/RADAR Digital Elevation Model (DEM) was created from fusing three existing DEMs of the lunar South Pole with 1 km pixel resolution [10] and was used as the base DEM for our first synthetically enhanced example. The Kaguya dataset used was a 250 m pixel resolution DEM of the lunar South Pole region which, although noisy, had no significant artifacts and was used to compare to the enhanced Clementine model. NASA's LRO LOLA instrument is continuing to obtain high resolution lunar topographic data [27] which is expected to provide higher resolution elevation models. However the publically available high resolution LRO DEMs obtained during this research were incomplete or contained deep score-like artifacts (lines across the DEM, see Figure 10, right) joining high resolution strips. This data set was used to create a second synthetically enhanced model and to create a non-enhanced model to compare with both the enhanced models.

### B. *Creating the Clementine/RADAR Enhanced Model*

An 1854×1854 pixel base DEM with 1 km horizontal resolution and 1 m vertical resolution was generated by Mullard Space Science Laboratory [28] by fusing three existing DEMs; the Clementine stereo DEM, the Clementine LIDAR DEM and the J-L Margot Goldstone RADAR DEM. The central 1025×1025 region of the fused DEM was extracted to form the base DEM for a synthetically enhanced model which is used to demonstrate and evaluate the surface modeling techniques described in the preceding sections. The central region was defined at higher resolution than the rest of the DEM but also contained noise, spikes and dips. There were some areas that contained unknown values and other areas that had been filled using basic interpolation. Pixels that could be identified as unrealistic spikes or dips were set to be unknown and noise in the central RADAR region was removed with a Gaussian filter. Many of the gaps in the central region of the terrain correspond to shadowed craters so a GUI was used to manually define crater shaped holes to be filled as craters and the remaining gaps were filled with fractal terrain. Figure 7 shows three stages of the DEM processing from the central region of the DEM.

Figure 7: DEM Processing; the original DEM (left), crater filled (center) and fractal hole filled (right)

A multi-resolution model was generated from the enhanced Clementine/RADAR DEM with the target landing side near the South Pole on the rim of Shackleton crater fractally expanded eleven times using the DEM expansion technique from section IV.A. The resolution of the landing site is $2^{11}$ (2048) times greater than the base DEM ranging from 1 km per pixel at the outer edges down to approximately 50 cm per pixel at the target landing site.

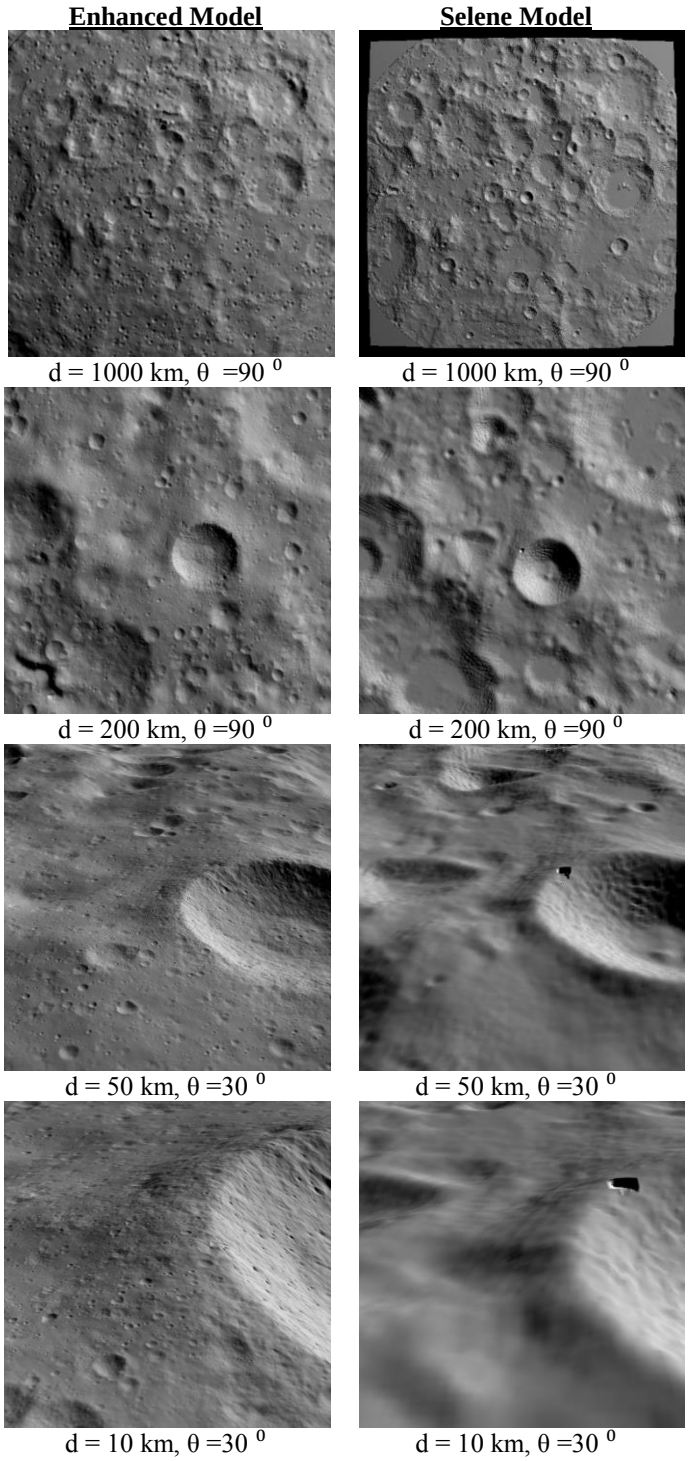


Figure 8: Enhanced 1 km DEM (left) comparisons with unenhanced 250 m Selene model (right).

Randomly generated craters defined at scales not present in the original DEMs were generated with a heavily cratered diameter distribution of $N_{cum}=cD^{-2}$ for craters between 1 m and 1000 m and added to the highest resolution layer that the entire crater could be added. Shackleton crater was replaced with a synthetic crater which reduced the fractal expansion factor from 2048 to 128 in the highest resolution layer resulting in a significantly sharper crater as shown in Figure 6. Finally the array of DEMs was converted into a multi-resolution polygon mesh.

### C. *Enhanced Model Comparison*

The Selene South Pole DEM with vertical resolution 0.3 m and horizontal resolution 250 m was converted into a polar stereographic DEM which was used to create a single resolution mesh model that could be rendered in the same way as the Clementine/RADAR enhanced model. There is some low level noise in this data and there is an artifact on the rim of Shackleton crater, however there were no significant gaps. Figure 8 shows a sequence of images comparing the two models with the left column images from the synthetically enhanced Clementine/RADAR DEM and the right column from the Selene model. The enhanced model base DEM has gaps and four times less resolution than the Selene comparison model, but although it is clear that the models have many differences, the proposed technique can fill the gaps appropriately and then increase the resolution of a section of the model with representative terrain by a factor of 512 greater than the 250 m Selene model.

A second comparison model was created from the LRO, LOLA sensor data with horizontal resolution of 80 m. This DEM is marked by deep scored line artifacts throughout caused by errors between the merged strips of terrain data obtained from the spacecraft sensor. Figure 9 shows the Clementine/RADAR enhanced model of Shackleton crater and the equivalent view from the LRO model.

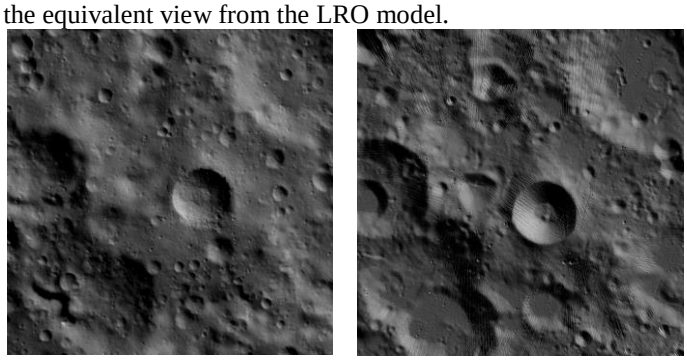

Figure 9: Enhanced 1km DEM (left) comparison with LRO 80 m model (right) 200 km above Shackleton crater

### D. *LRO Enhanced Model Comparison*

A second synthetically enhanced model was created and evaluated from LRO data. A 960 m resolution LRO DEM was obtained with no significant artifacts and fractally expanded ten times with small synthetic craters added in a lunar diameter distribution. This model was used to compare the fractally expanded low resolution DEM with the high resolution DEM with artifacts. Figure 10 shows two near surface images of Malapert ridge which is a well illuminated potential landing site near the lunar South Pole. The LRO

80 m DEM model with artifacts and limited resolution can be contrasted with the 960 m enhanced DEM model showing that the synthetically enhanced model would be superior for testing vision based landers because it has significantly higher resolution and no artifacts.

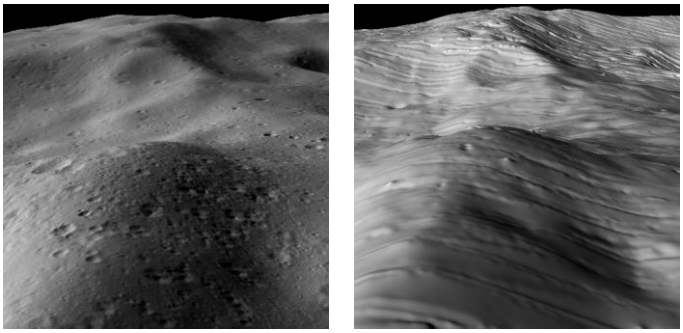

Figure 10: LRO 960 m enhanced DEM (left) comparison with LRO 80 m DEM of Malapert ridge

E. *Slope distribution evaluations*

Slope distributions were calculated to evaluate consistency at different resolutions within the hierarchical model and to compare against lunar slope distributions. Figure 11 shows cumulative slope frequency distributions for the 11 DEM layers in the enhanced multi-resolution model which shows the percentage of terrain greater than a given slope angle calculated with the Horn algorithm [29]. There is a reasonably consistent slope distribution at different resolutions, with fewer slopes greater than 10º in the highest resolution layers and in the initial DEM. This is possibly because the initial DEM is missing high-frequency terrain data and craters smaller than 1 m in diameter are not included. Slopes in the 3.91 m to 31.15 m resolution range are significantly higher than lower resolutions which are more closely related to the base DEM roughness.

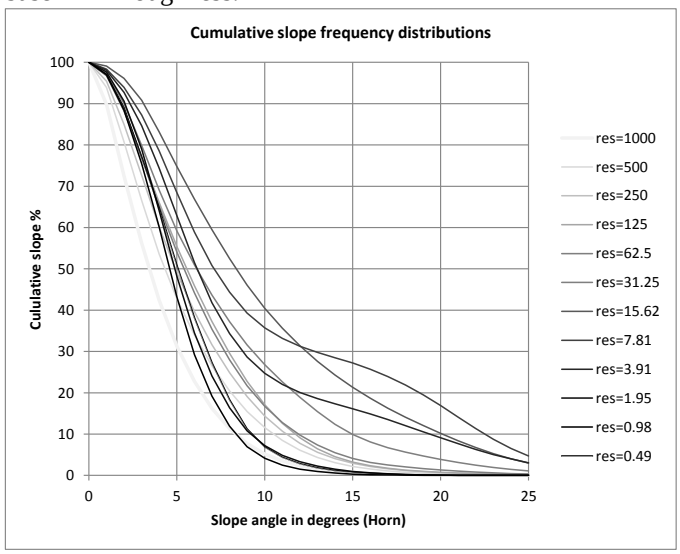


Figure 11: Cumulative slope frequency distributions for the 11 DEM layers in the enhanced multi-resolution model

The slope distribution of the enhanced model can be tuned by adjusting the crater distributions, the degradation parameters and the fractal dimension used for both the surface expansion and the crater overlays. The roughness of the initial base DEM can be increased by overlaying a fractal surface limited to a defined height range if it is believed that the initial DEM has lost high-frequency terrain data during its creation.

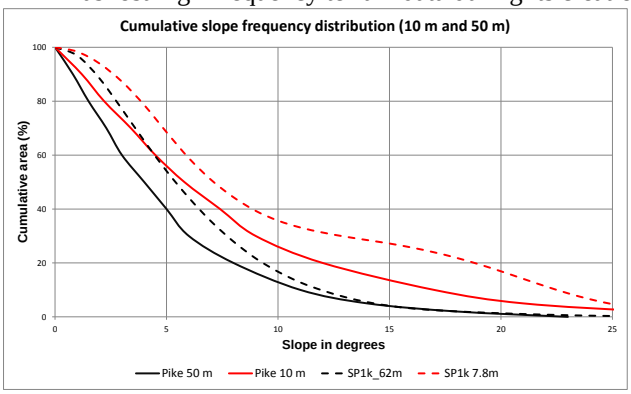


Figure 12: Comparing cumulative slope frequency distributions of a synthetically enhanced model and lunar data [Pike 1969].

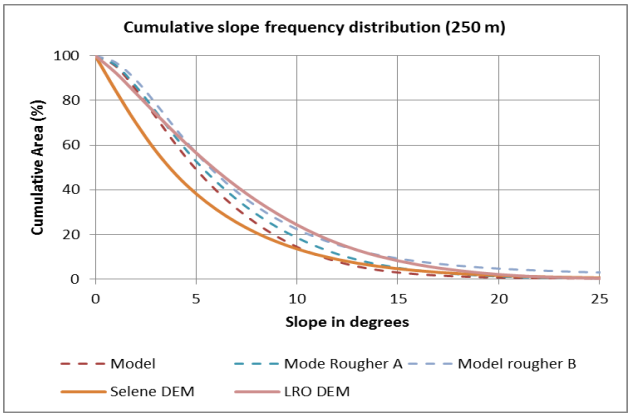


Figure 13: Cumulative slope frequency distributions synthetically enhanced models and the Selene and LRO DEMs.

Figure 12 compares lunar slope distributions for "rough upland" terrain calculated by Pike from a NASA study during the Apollo period [30] with the enhanced model at similar resolutions of around 10 m and 50 m. The lunar data is consistently less rough than the synthetic South Pole model so it is possible that our model is too rough at these high spatial resolutions but the lunar data is for generally "rough upland" which is unlikely to be as rough as the South Pole region.

Figure 13 compares slope distributions of three versions of the synthetically enhanced model with Selene and LRO DEMs at 250 m resolution. The three versions are the model described in section V.B, a rougher version (A) with less crater erosion and (B) with a high-frequency fractal overlay applied to the base DEM with fractal dimension of 2.2 and elevation range of 5000 m. This shows that the slope distribution of the enhanced model is within the slope range of the two DEMs at that resolution and could be tuned to match if desired.

Figure 14 shows the radially averaged power spectrum for both the synthetically enhanced and Selene models at 250 m resolution. This measures the amount of structure at a given

physical scale, regardless of the direction. The fact they are very similar demonstrates that the synthetically enhanced terrain is not significantly more rough or smooth than the real terrain at any spatial frequency.

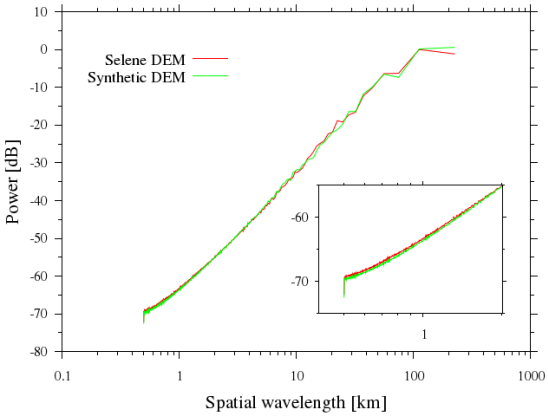


Figure 14: Comparison of radially averaged power spectrum for synthetically enhanced and Selene models at 250 m resolution.

### F. *Feature tracking*

Rendered images from the enhanced Clementine/RADAR and Selene models were supplied to an optical navigation feature tracking application [31] to evaluate the response of the models to a realistic vision guidance image processing system. Features [32] are identified and tracked in a sequence of images and the motion of these tracks can be used for a variety of optical navigation algorithms [33].

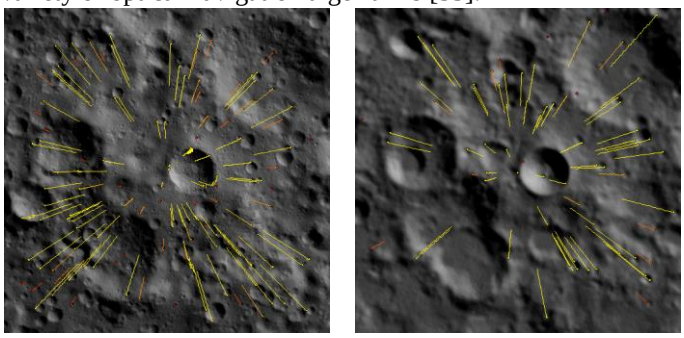

Figure 15: Tracking features on the synthetically enhanced South Pole model (left) and the Selene model (right). The lines represent features tracked across multiple images shown in the final image in the sequence.

The 250 m Selene model contained noise which was originally picked up by the feature extraction algorithm so was smoothed with a seven pixel width Gaussian filter. High frequency terrain data was replaced by overlaying a fractal DEM scaled to 1000 m in range. The feature tracks are shown pictorially in Figure 15 with each line representing one feature tracked in a sequence of images showing that features can be extracted and tracked for both the Selene and the enhanced models. The enhanced model generates more tracks, possibly because it contains more surface information. Tracks can be generated throughout the decent sequence with the feature tracking continuing successfully across resolution jumps which demonstrates that the artificial models do not contain unnatural artifacts that get detected by the feature tracking algorithm.

## VI. Conclusion

We have described original surface modeling techniques to simulate the terrain of rocky cratered surfaces for planetary lander simulation with an original crater model that can be used to simulate crater saturated surfaces. Comparisons between the Clementine/RADAR enhanced model and the Selene and LRO models show the effectiveness of the crater model, fractal expansion, terrain gap filling and feature replacement techniques for creating multi-resolution models with a high resolution target landing site region from low-resolution base DEMs. The excessively curved rim of the expanded Shackleton crater shows a limitation with repeated surface expansion that can be alleviated through crater replacement.

The cratered surfaces generated can be controlled by the diameter and age distributions used and by the fresh crater depth and rim height to diameter relationship. The roughness of the synthetic terrain can be adjusted by the fractal parameters used in the surface expansion and crater overlays. The crater model is only applicable to simple craters and so is limited to modeling lunar craters smaller than 10-15 km in diameter but larger, complex craters are generally defined in the base DEM.

The slope distributions and the power spectrum show that the synthetically enhanced terrain has similar slope distribution characteristics to the lunar data but the base DEMs used may be too smooth. Higher resolution layers more closely approximate the lunar data slope distributions where the terrain roughness is dependent on the crater model parameters, crater diameter and age distributions and the fractal dimension specified during surface expansion.

The suitability of the multi-resolution models to test lander navigation and guidance systems was demonstrated with feature tracking which showed the advantage of the enhanced model which could track features to the resolution required for a complete lander descent. It also showed that the feature extraction algorithm does not unduly pick up feature points on resolution borders or when the resolution moves to a higher resolution region within the multi-resolution model.

The surface modeling techniques presented have focused on a lunar South Pole lander but the same techniques could be applied to any base DEM of a rocky cratered surface to generate a multi-resolution model to simulate a landing descent because the crater model profile and distributions could be adjusted to suit properties found on different planetary bodies.

## VII. Further Work

Boulder simulation is required to model the landing site regions for hazard detection and will be presented in future research. Further work being considered is to obtain higher resolution LRO DEMs when they become available that do not contain artifacts and use these to create more realistic

multi-resolution models of the lunar South Pole to support the Lunar South Pole Lander studies. The realism of craters on steep slopes could be improved by applying realistic slope based crater distributions and by modifying the crater model to include slope based degradation.

## ACKNOWLEDGMENT

The authors would like to acknowledge the support of the European Space Agency for the work described in this paper, in particular ESA project managers Olivier Dubois-Matra, Salvatore Mancuso and Stein Strandmoe. Some of the work described in this paper was partly funded by ESA Contract No. 20858/07/NL/EK "PANGU Extension" led by the University of Dundee.

## REFERENCES

[1] S. Parkes, M. Dunstan, I. Martin, M. McCrum and O. Dubois-Matra, "Testing Advanced Navigation Systems for Planetery Landers and Rovers," in *In Proceedings of the 60th International Astronautical Congress*, Daejeon, Republic of Korea, Oct. 2009.

[2] S. Strandmoe, T. JeanMarius and S. Trinh, "Toward a vision based autonomous planetary lander," in *AIAA Guidance, Navigation, And Control Conference*, 1999, Vol. 1-3, Ch. 197, pp.1134-1144.

[3] A. Pradier, R. Fisackerly, B. Houdou, C. Phillipe, J. Carpenter, D. De Rosa, S. Espinasse, B. Gardini and N. Henn "The First European Lunar Lander and the ESA-DLR Approach to its Development," in *In Proceedings of the 61st International Astronautical Congress*, Prague, 2010, pp2962-2967.

[4] R. Fisackerly, J. Carpenter, D. De Rosa, A. Pradier, C. Philippe, and B. Gardini and "The European Lunar Lander: Robotic Operations in a Harsh Environment", *Moon*, 2011.

[5] V. Miller, D, Pirker, R. De La Torre, C. Vaughn, B. Hawley, R. McHenry, C. Dusold and J. Gasvoda, "Lunar lander mission evaluation lab," *Aerospace conference, 2009 IEEE*, vol., no., pp.1-9, 7-14 March 2009.

[6] H. Noda, H. Araki, S. Goossens, Y. Ishihara, K. Matsumoto, S. Tazawa, N. Kawano and S. Sasaki (2008), "Illumination conditions at the lunar polar regions by KAGUYA(SELENE) laser altimeter", Geophys. Res. Lett., 35, 35, pp. 1-5, 2008.

[7] H. Melosh, *Impact Cratering – A Geologic Process*, Oxford University Press, 1989.

[8] G. Heiken, D. Vaniman, B.French, "The Lunar Sourcebook: A Users guide to the Moon", *Cambridge University Press*, 1991, ISBN 0-521-33444-6.

[9] S. Sqyres, C. Howell and M. Liu, "Investigation of Crater 'Saturation' Using Spatial statistics", Icarus 125, Article No. IS965560, 1997, pp 67-82.

[10] W. Hartmann, "Planetary Cratering 1. The Question of Multiple Impactor Populations: Lunar Evidence", Meterotics, No. 30, 1995, pp 451-467.

[11] H. Ross, "A Simplified Model for Lunar Crater Erosion", J. Geophys. Res., Vol.73, No. 4, pp1343—1354, 1968.

[12] L. Soderblom, "A Model for Small-Impact Erosion Applied to the Lunar Surface," J. of Geophys. Res., Vol 75, No.14, pp265-261 (1970).

[13] B. Mandelbrot, *The Fractal Geometry of Nature*, New York: WH Freeman & Co., 1988.

[14] G. Miller, "The definition and rendering of Terrain Maps", *Proc. 13th Ann. Conf. Computer Graphics and Interactive Techniques (SIGGRAPH '86)*, Vol. 20. pp.39-48, 1986.

[15] F. Belhadj, "Terrain modeling: a constrained fractal model", in *5th International conference on CG, virtual reality, visualisation and interaction in Africa*, pp. 197–204. ACM, Grahamstown, South Africa, 2007.

[16] D. Esbert, F. Musgrave, D. Peachey, K. Perlin and S. Worley, *Texturing & Modelling A Procedural Approach*, Third Edition, Morgan Kaufmann, 2003, ch. 12.

[17] S. Vasudevan, F. Ramos, E. Nettleton, H. Durrant-Whyte, A. Blair, "Gaussian Process modeling of large scale terrain", *IEEE International Conference on Robotics and Automation*, 1047-1053, 2009.

[18] H. Zhou, j. Hsun, G. Turk, J. Rehg. "Terrain Synthesis from Digital Elevation Models", *IEEE Trans. Visualization and Computer Graphics*, 13, 4, 834-848, 2007.

[19] U. Shankar, T. Criss, W. Shyong, and D. Adams, "Lunar Terrain Surface Modeling for the ALHAT Program," *Aerospace Conference, 2008 IEEE* , vol., no., pp.1-10, 1-8 March 2008.

[20] S. Qinghua, Z. Yan, W. Falin, X. Chunming, C. Yanlong, "Simulation of high resolution lunar's Sinus Iridum terrain," in *6th IEEE Conference on Industrial Electronics and Applications*, 2011, pp 2589 – 2592.

[21] X. Huang, X. Jiang, T. Yu, H. Yin, "Fractal-Based Lunar Terrain Surface Modeling for the Soft Landing Navigation," in *2nd International Conference on Intelligent Computation Technology and Automation*, vol. 2, pp.53-56, 2009.

[22] T. McGetchin, M. Settle and J. Head, "Radial thickness variation in impact crater ejecta: Implications for lunar basin deposits", Earth Planet. Sci. Lett. 23: 271-274, 1974.

[23] H. Peitgen and D. Saupe, *The Science of Fractal Images*, 1988 Springer-Verlag New York.

[24] M. Rosiek, R. Kirk and E. Howington-Krauss, "Digital Elevation Models derived from small format Lunar images", ASPRS 2000, ASPRS, Washington D.C.

[25] J.L. Margot, D.B. Cambell, R.F. Jurgens and M.A. Slade, "Topography of the Lunar Poles from Radar Interferometry: A Survey of Cold Trap Locations," Science, 284: 1658-1660, 1999.

[26] H. Riris et al , "The Lunar Orbiter Laser Altimeter (LOLA) on NASA's Lunar Reconnaissance Orbiter (LRO) Mission," in *Conference on Lasers and Electro-Optics/International Quantum Electronics Conference*, Optical Society of America, 2009, paper CFJ1.

[27] D. Smith et al., "Initial observations from the Lunar Orbiter Laser Altimeter (LOLA)". Geophysical Research Letters. 37, 2010.

[28] J-P. Muller, S-Y. Lin and J-R. Kim, "Final Report on Martian and Lunar DEMs", in *WP4.1 of the PANGU Enhancement project*, ESA, 2008, unpublished.

[29] B. Horn, "Hill shading and the reflectance map", *Proc. IEEE*, 69(1), 14-47, 1981.

[30] R. Pike, "Lunar terrain and traverse data for Lunar roving vehicle design study", Lunar and Planetary Institute, Houston, 1969.

[31] M. Dunstan, S. Parkes and S. Mancuso, "Visual Navigation Chip for Planetary Landers," in *Data Systems in Aerospace*, Edinburgh, Scotland, May 2005.

[32] C. Harris and M. Stephens, "A Combined Corner and Edge Detector," in *In Proceedings of The Fourth Alvey Vision Conference*, University of Manchester, UK, Aug. 31 1988, pp. 147-151.

[33] N. Rowell, S. Parkes, M. Dunstan, "Image processing for near Earth object based vision guidance system," *IEEE Trans. on Aerospace and Electronic Systems, vol.49, no.2, 2013.*

**Iain Martin** Dr. Iain Martin is a lecturer at the Space Technology Centre at the University of Dundee. His research interests include planet surface simulation for autonomous spacecraft, testing of vision based guidance systems, 3D graphics and SpaceWire networks.

**Steve Parkes** Prof. Steve Parkes is a Chair of Spacecraft Electronic Systems and director of the Space Technology Centre, School of Computing, and University of Dundee, Scotland. Professor Parkes leads research work on the design and development of spacecraft on-board data-handling networks (SpaceWire), planet surface simulation and autonomous lander navigation, and digital signal and image processing for satellites. Professor Parkes is a member of the IEEE.

**Martin Dunstan** Dr. Martin Dunstan is a postdoctoral research assistant working on the visualization of simulated planet surfaces and spacecraft using OpenGL, simulation of LIDAR images for GNC landing and orbital rendezvous man oeuvres, and the development of a hardware chip for feature extraction and tracking to support vision-guided planetary landers.